OPEN ACCESS
IOP Publishing | Songshan Lake Materials Laboratory
Materials Futures
Mater. Futures 3 (2024) 035102 (11pp)
https://doi.org/10.1088/2752-5724/ad50f1

Enhancing performance and longevity of solid-state zinc-iodine batteries with fluorine-rich solid electrolyte interphase

Yongxin Huang[1], Yiqing Wang[1], Xiyue Peng[1], Tongen Lin[1,2], Xia Huang[1], Norah S Alghamdi[1,3,4], Masud Rana[1], Peng Chen[1], Cheng Zhang[1,*], Andrew K Whittaker[1], Lianzhou Wang[1,2] and Bin Luo[1,*]

[1] Australian Institute for Bioengineering and Nanotechnology (AIBN), The University of Queensland, Brisbane, QLD, 4072, Australia
[2] School of Chemical Engineering, The University of Queensland, Brisbane, QLD, 4072, Australia
[3] School of Chemistry and Molecular Biosciences, Faculty of Science, The University of Queensland, Brisbane, QLD, 4072, Australia
[4] Department of Chemistry, Faculty of Science, Imam Mohammad Ibn Saud Islamic University (IMSIU), Riyadh 11564, Saudi Arabia

E-mail: c.zhang3@uq.edu.au and b.luo1@uq.edu.au

Received 9 April 2024, revised 19 May 2024
Accepted for publication 26 May 2024
Published 17 June 2024

Abstract

Rechargeable zinc-iodine (ZnI_2) batteries have gained popularity within the realm of aqueous batteries due to their inherent advantages, including natural abundance, intrinsic safety, and high theoretical capacity. However, challenges persist in their practical applications, notably battery swelling and vulnerability in aqueous electrolytes, primarily linked to the hydrogen evolution reaction and zinc dendrite growth. To address these challenges, this study presents an innovative approach by designing a solid-state ZnI_2 battery featuring a solid perfluoropolyether based polymer electrolyte. The results demonstrate the formation of a solid electrolyte interphase layer on zinc, promoting horizontal zinc growth, mitigating dendrite penetration, and enhancing battery cycle life. Moreover, the solid electrolyte hinders the iodine ion shuttle effect, reducing zinc foil corrosion. Symmetric batteries employing this electrolyte demonstrate excellent cycle performance, maintaining stability for approximately 5000 h at room temperature, while solid-state ZnI_2 batteries exhibit over 7000 cycles with a capacity retention exceeding 72.2%. This work offers a promising pathway to achieving reliable energy storage in solid-state ZnI_2 batteries and introduces innovative concepts for flexible and wearable zinc batteries.

Supplementary material for this article is available online

Keywords: zinc-iodine battery, solid electrolyte, zinc metal anode, electrolyte interphase, shuttle effect

* Authors to whom any correspondence should be addressed.

1. Introduction

The surging demand for energy storage driven by applications such as electric vehicles and large-scale energy storage has exposed the limitations of lithium-ion batteries in meeting market requirements. As a result, there is a growing focus on alternative, safer and lower-cost energy storage technologies. Among these alternatives, rechargeable aqueous zinc batteries have attracted considerable attention due to their safe and abundant resource availability [1]. The high theoretical capacity (820 mAh g^{-1}) and environmentally friendly properties of zinc, coupled with its favorable redox potential, position it as a strong contender in the realm of metal batteries [2, 3]. Iodine has emerged as a promising cathode material for zinc metal batteries due to its promising theoretical capacity (211 mAh g^{-1}) and widespread abundance in the earth's crust [4]. However, the limited lifespan of zinc iodine (ZnI_2) batteries remains a significant challenge to their further development [5]. During the operation of rechargeable aqueous zinc metal batteries, the pH value of the electrolyte undergoes constant fluctuations [6]. Upon reaching a certain threshold, the battery forms a mesophase passivation layer containing some impurities like ZnO and $Zn(OH)_4^{2-}$ [7, 8]. The thermodynamic instability of the zinc electrode in the aqueous electrolyte always leads to the evolution of hydrogen, causing the battery to swell and ultimately fail [9–11]. Moreover, in aqueous electrolytes, iodine cathodes typically engage in reversible redox reactions involving triiodides, iodides, and polyiodides ($I_3^-/I^-/I_5^-$) [12]. The ZnO and $Zn(OH)_4^{2-}$ passivation layer may further interact with triiodide, compounding the adverse effects on the zinc anode [13]. Therefore, mitigating these parasitic side reactions on the Zn surface is imperative for achieving long-life rechargeable ZnI_2 batteries.

Different strategies have been explored to address these issues, including surface decoration and artificial coating of zinc anodes and/or separators [9, 14–16]. However, as water remains a key participant in side reactions in aqueous zinc metal batteries, the problems related to H_2O, with its limited electrochemical window (EW), remain largely unresolved [9]. A potential solution is to replace liquid electrolytes with solid electrolytes, eliminating water-related side reactions and enhancing safety and thermal stability [17–19]. In this context, the design of an all-solid-state ZnI_2 battery without liquids holds substantial promise for improving battery safety and lifespan. Solvent-free polymer electrolytes stand out as strong candidates due to their inherent flexibility, mechanical strength, and high electrochemical stability [7, 20, 21].

In this study, we report a novel class of fluorinated block copolymer as solid electrolyte for the development of all-solid-state ZnI_2 batteries with extended lifespans. Our findings reveal that the zinc metal anode cycled in such solid electrolyte develops a stable fluoride-rich solid electrolyte interphase (SEI) layer, promoting zinc deposition in a horizontal direction and preventing the growth of hazardous zinc dendrites that could compromise the separator and lead to battery failure. Additionally, this solid electrolyte effectively mitigates the I_3^- shuttle issue and substantially extends battery cycle life, as illustrated in figures 1(a) and (b). Symmetric cells assembled with this solid electrolyte demonstrate stable plating and stripping for approximately 5000 h at 0.2 mA cm^{-2}. The full ZnI_2 battery exhibits extended operational durations, impressive rate performance, and nearly 100% coulombic efficiency for over 7000 cycles (more than 10 000 h) at 0.5 C. This electrolyte demonstrates excellent rate performance, even at an ultrahigh current density of 20 C, the battery can still deliver a reversible capacity of 79.8 mAh g^{-1}. These results underscore the significant commercial potential of this all-solid-state battery. This study opens a new avenue of designing fluorine-containing solid-state polymer electrolyte for the next-generation ZnI_2 batteries with dendrite-free Zn metal anodes and ultra-long battery lifespans.

2. Experimental methods

2.1. Materials synthesis

The monohydroxy perfluoropolyether (PFPE-OH, ∼2000 g mol^{-1}, CAS number: 126066-30-6) was provided by the Chemours Company. The radical initiator 2,2′-azobis(2-methylpropionitrile) (AIBN) was recrystallized twice from methanol before use. The reversible addition-fragmentation chain-transfer (RAFT) agent, 2-(Butylthiocarbonothioylthio)propionic acid (BTPA), was prepared according to a published procedure [22]. Oligo(ethylene glycol) methyl ether acrylate (OEGA, M_w = 480 g mol^{-1}, Sigma-Aldrich) was passed through basic alumina columns to remove inhibitors before use. All other chemicals were purchased from Sigma-Aldrich and used as received.

Syntheses of PFPE-based polymer (PF): BTPA-PFPE macro-RAFT agent was synthesized by a N-(3-(dimethylamino)propyl)-N′-ethylcarbodiimide hydrochloride and 4-(dimethylamino) pyridine (EDCl/DMAP) coupling. Then the PF polymer electrolyte, poly$(OEGA)_{10}$-PFPE (PF), was synthesized via RAFT polymerization. BTPA-PFPE macro-RAFT agent (2000 mg, 0.90 mmol), OEGA (4551.9 mg, 9.483 mmol), and AIBN (29.5 mg, 0.18 mmol) were dissolved in trifluorotoluene (10 ml) and sealed in a 50 ml flask fitted with a magnetic stirrer bar. The solution was then deoxygenated by purging with argon and then reacted at 70 °C for 6 h. Unsealing to stop the reaction, the conversion of monomer (OEGA) to polymers was determined immediately by ^{1}H NMR using the crude solution mixtures (figure S1). To remove the residual monomer, the reaction solution was precipitated into hexane/diethyl ether mixed solvent and redissolved in THF three times. The precipitate was then vacuum dried at 40 °C for 48 h to obtain a yellow viscous solid. The product (PF) was confirmed by ^{1}H and ^{19}F NMR (figures S2(a) and (b)).

Syntheses of Solid-state electrolyte (PFZ): 30 mg of the obtained PF were dissolved in 1.5 ml of acetonitrile (ACN), followed by the addition of 1 ml of a 2 M aqueous solution of zinc sulfate. The molar ratio of EO/Zn^{2+} in the solid

electrolyte was estimated to be 2/11, as shown in table S1. The resulting mixture was placed on a stirring plate at room temperature and stirred magnetically for 1 h. Subsequently, the solution was transferred to a vacuum oven and dried under vacuum overnight at 100 °C to yield a sample denoted as PFZ. The weight loss proportion of the zinc salt and PFZ from room temperature to 800 °C was analyzed via thermal gravimetric analysis, as depicted in figure S3. During the heating process of 0 °C–100 °C, the free water in zinc sulfate heptahydrate is consumed and the new peak of PFZ in the 200 °C interval is because part of the free water is not completely drained during the overnight heating process. The weight loss of PFZ in the range of 700 °C–900 °C should be caused by the continuous decomposition of PF and zinc salts.

2.2. Material characterization

Both ^{1}H and ^{19}F NMR spectra were acquired in deuterated chloroform ($CDCl_3$) at 25 °C on a Bruker Avance 400 MHz (9.4 T) spectrometer. All ^{1}H NMR measurements were conducted under the following conditions: 90° pulse width 14 μs, relaxation delay 1 s, acquisition time 4.1 s, and 32 scans. ^{19}F NMR spectrum was acquired under following conditions: A 90° pulse width of 15 μs, relaxation delay 1 s, acquisition time 0.73 s, and 64 scans. X-ray photoelectron spectroscopy (XPS) was performed to gather information on the surface composition of the zinc electrode after cycling. To examine both the surface and subsurface composition of the zinc foil and electrolyte, we employed argon gas etching at different depths. To identify the phase and crystal structure changes on the surface of the Zn electrode after cycling in different environments, x-ray diffraction (XRD) analysis was performed. The measurements were conducted using a Bruker x-ray diffractometer (Bruker, D8-Advance x-ray diffractometer, Cu Kα, $\lambda = 0.15406$ nm) at a scan rate of 5° min^{-1}. Raman spectra were obtained using the Renishaw Raman microscope and spectrometer with laser wavelengths of 514 nm. The surface and cross-sectional morphologies of zinc foils were characterized by scanning electron microscopy (SEM). All electrodes were dried overnight in a vacuum oven at 50 °C before characterization. UV–vis is a good quantitative method to explore the concentration changes of I_3^- after separation between GF and PFZ.

2.3. Electrochemical measurements

Electrochemical measurements were conducted with standard 2032 coin cells at room temperature. For symmetric cells, a pair of identical Zn foils (Zn//Zn) served as both electrodes, while the aqueous zinc sulfate electrolyte and solid electrolyte were used as electrolytes for the control group. Galvanostatic discharge and charge tests were performed at various current densities using the LAND battery test system.

For full cells, the cathode material was prepared by mixing nitrogen-doped CMK-3 carbon with I_2 (CMK-N@I_2) in a dry room to obtain a homogeneous mixture. The mixture was then sealed in a Pyrex tube and heated at 60 °C for 12 h, followed by cooling to room temperature to facilitate *in situ* deposition of I_2 within the pores of nitrogen-doped CMK-3. The ratio of mesoporous carbon to iodine was maintained at 4:6. A slurry containing CMK-N@I_2, Super P, PVDF with a mass ratio of 7:2:1 in N-methylpyrrolidone was uniformly mixed and cast onto the carbon paper current collector. Subsequently, the resulting cathode was dried in a vacuum oven at 40 °C overnight for 12 h. The average areal loading per cathode was approximately 1–1.3 mg cm^{-2} [2]. Zn//PFZ//Zn cells were cycled at 0.5 C with the voltage range set between 0.4 −1.6 V.

Cyclic voltammetry (CV), linear sweep voltammetry (LSV), electrochemical impedance spectroscopy (EIS), and Tafel measurements were conducted using a two-electrode configuration at electrochemical workstation (Biologic). CV testing covered a voltage range from 0.2–1.8 V, and the EIS spectra were collected within a frequency range of 10^{-1}–10^{5} Hz. For the LSV test, a stainless-steel foil served as the working electrode, and a Zn foil was used as the counter/reference electrode, with a fixed scanning rate of 0.5 mV s^{-1}. In the Tafel test, the working and counter/reference electrodes were Zinc foils, and potentiodynamic polarization curves were obtained to illustrate the corrosion behaviors of zinc metal, with the scanning rate of 1 mV s^{-1}.

3. Results and discussion

3.1. Synthesis and electrochemical performance of the solid electrolytes

The synthesis of solid electrolytes mainly involves two steps. The first step is the synthesis of a perfluoropolyether (PFPE)-containing polymer (PF). The successful synthesis of the polymer electrolyte was confirmed by NMR spectra. The ^{1}H and ^{19}F of PF after purification align well with previous reports [23, 24]. Specifically, in the ^{1}H spectrum (figure S2(a)), the methylene protons (2 H, −CH2O−) adjacent to the ester groups of the OEGA and the terminal ether oxygen of PFPE are observed at ∼4.2 ppm (H6) and ∼4.6 ppm (H5), respectively. This observation is corroborated by the ^{19}F NMR spectrum (figure S2(b)) of PF, where the most intense peak F1 at ∼− 80 ppm originates from the difluoromethylene (2 F, −CF2−) and trifluoromethyl group (3 F, −CF3) within the PFPE segment of the copolymer. The NMR spectra validates the successful synthesis of the polymer electrolyte, and the comprehensive structural characteristics of PF are summarized in table S2. After synthesizing the PF polymer, an ion exchange method (the second step) was used to introduce Zn ion (Zn^{2+}) into this PF, yielding a zinc-rich solid-state electrolyte. Briefly, PF dissolved in ACN was added to 2 M zinc sulfate ($ZnSO_4$) aqueous solution drying in the vacuum oven overnight at 100 °C. The as-obtained PF & $ZnSO_4$-based solid-state electrolyte (PFZ) was a gel-like material (insert of figure S4). SEM image (figure S4) of PFZ reveals a smooth surface morphology. To further confirm the successful fusion of PF and $ZnSO_4$, the elemental composition of PFZ was

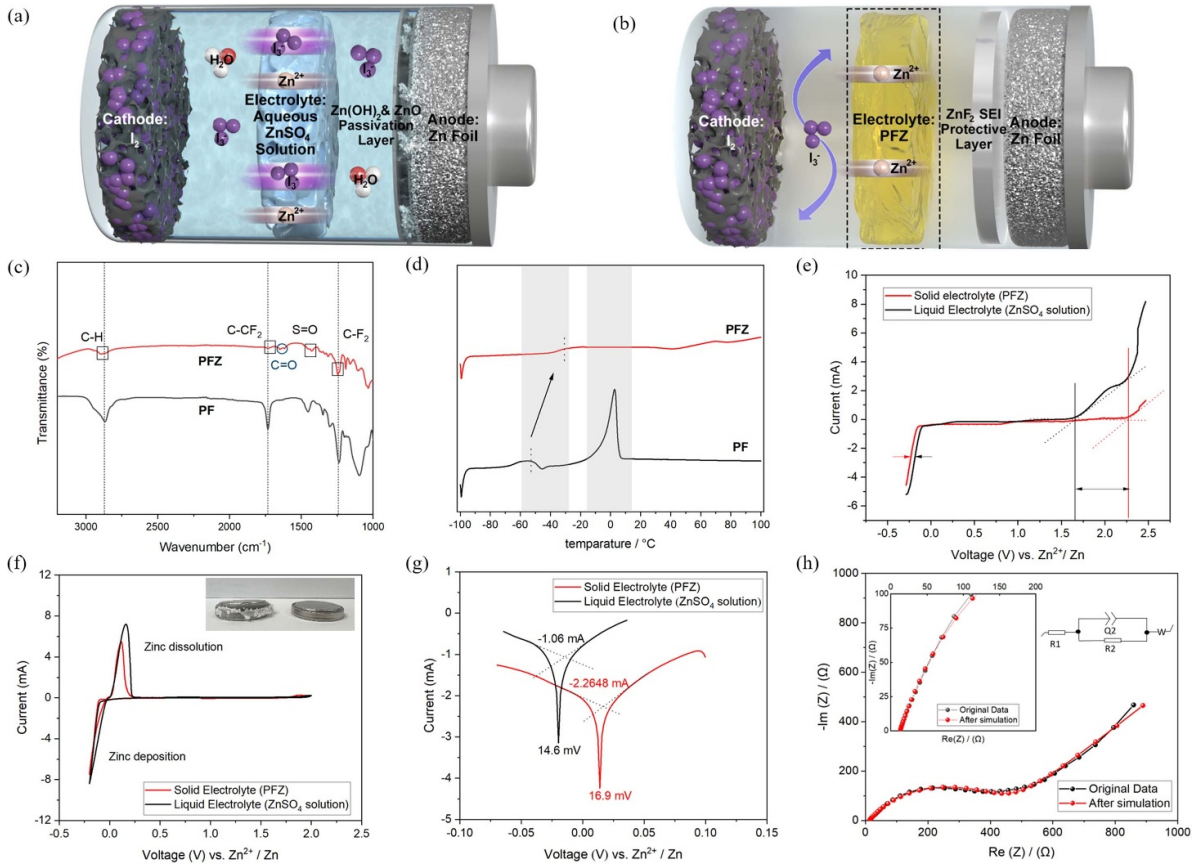

Figure 1. Schematic illustration of ZnI_2 batteries with (a) aqueous $ZnSO_4$ solution and (b) solid PFZ as electrolyte. (c) FTIR spectra of PFZ and PF. (d) Tg comparison of PF polymer and PFZ. (e) LSV curves of the PFZ electrolyte and the liquid electrolyte (2 M aqueous $ZnSO_4$ solution electrolyte) using a two-electrode configuration (stainless steel foil as working electrode and Zn foil as reference and counter electrodes). (f) CV curves of Zn plating/stripping using two-electrodes configuration in PFZ (stainless steel foil as working electrode and Zn foil as reference and counter electrodes) and 2 M aqueous $ZnSO_4$ solution. Inset: Digital photos of the battery cycled in 2 M aqueous $ZnSO_4$ solution electrolyte and PFZ electrolyte. (g) Potentiodynamic polarization curves using two-electrode configuration (zinc foil as working electrode and another zinc foil as reference electrode and counter electrode) showing the corrosion behaviors on zinc metal. (h) EIS spectra of PFZ electrolyte and the fitting curve.

analyzed employing XPS. It was found that even after etching for 30 s (approximately 33 nm depth for PFZ), Zn 2p and S 2p originating from $ZnSO_4$ were still observable without any discernible impurities (figures S5–S8), indicating the successful insertion of Zn salts into the channels of PFZ, forming a zinc-based composite electrolyte. Additionally, new peaks corresponding to C=O bonds emerged in the C and O spectra, respectively (figure S8). Fourier transform infrared spectroscopy (FTIR) was employed to unveil the chemical bonds present on the surface of the synthesized PFZ, covering the wavelength range of 500–4000 cm^{-1} (figure 1(c)). The spectral regions observed at 1245 cm^{-1} and 1732 cm^{-1} can be attributed to the vibration of C-F and C-CF from PF, respectively, while the resonance at 1480 cm^{-1} can be assigned to the S=O chain of zinc salts, corresponding to the anionic group in zinc sulfate. This resonance may refer to the emergence of free Zn^{2+}, which could enhance the conduction process. The overlapping peaks in the range of 1200–1000 cm^{-1} likely correspond to the combination of free ions and higher aggregates [25]. Regardless of the salt concentration, the formation of ion pairs or advanced aggregates is inevitable [26]. As shown in the FTIR results, two new peaks belonging to C=O can be clearly observed at the positions of 1618 and 1645 cm^{-1}. This may be attributed to the coordination of Zn^{2+} ions with the lone pair of electrons on the oxygen atom, forming bonds between C=O and Zn^{2+}. Thus, XPS and FTIR spectroscopic analysis confirmed the complexation of zinc salts and PF. The interactions between polymers and metal ions were further investigated by measuring the glass transition temperature (Tg) using a differential scanning calorimeter [27]. As shown in figure 1(d), differential scanning calorimetry measurements of pure PF copolymer exhibits a T_g of −59.5 °C with an endothermic melting peak (T_m) between −20 and 10 °C, associated with glass-to-rubber relaxation and PEO domain melting, respectively [28]. Upon adding Zn salt, the T_g of PFZ increased to −35.6 °C with the complete disappearance of the melting peak. From the above material characterizations, the strong interaction between the polymer and the metal ions has changed the property of the polymer, which is supposed to impact the battery performance [29].

The EW of electrolytes is defined as the electric potential range in which the electrolytes are stable without being reduced and oxidized. As one of the most notable features, electrolytes with wide EW are desirable to expand the selection of electrodes for not only higher energy density but also longevity [30]. Therefore, EW gauges the extent of the electrolyte's oxidation and reduction capabilities, pivotal in evaluating battery performance [31]. EW is usually determined using LSV. Typically, the current at the working electrode is measured while the potential changes linearly from a lower potential to a higher potential. Figure 1(e) highlights that the PFZ solid electrolyte displays a broader EW than the 2 M $ZnSO_4$ aqueous solution. With oxygen evolution reaction and plating reaction at 2.07 V and −0.1 V, respectively, the solid electrolyte delivers an operating voltage window of about 2.17 V, which sufficiently matches most zinc metal battery cathodes.

CV analysis of both PFZ solid electrolyte and liquid electrolyte (figure 1(f)) reveals that the electrochemical stripping and plating process of Zn typically occurs at around 0 V (vs. Zn^{2+}/Zn). Furthermore, the anodic and cathodic peaks demonstrate excellent current response and reversibility, highlighting the robust electrochemical deposition/dissolution performance of Zn. Failure of Zn batteries primarily results from the hydrogen evolution reaction (HER) and corrosion reactions of Zn anode in aqueous electrolytes. Therefore, the electrochemical stability of electrolytes and efficiency of zinc stripping and plating are important characteristics in evaluating electrolytes [32]. Since water serves as the solvent for $ZnSO_4$ solution, its electrochemical stability was initially assessed in the voltage range of −0.5–2.5 V. The results indicate that the electrochemical stability window of water is limited to −0.05–1.65 V (figure S9). Notably, the galvanizing reactions taking place in the 2 M $ZnSO_4$ aqueous electrolyte extend beyond this window, leading to the occurrence of HER. As shown in the digital photos (inset of figure 1(f) left), battery cycled in aqueous $ZnSO_4$ solution exhibits flatulence with some zinc salt precipitation, suggesting the hydrogen gas causes the battery expansion and failure eventually. In contrast, solid-state batteries with PFZ electrolyte operate within the same EW, effectivity devoid the hydrogen production (inset of figure 1(f) right). Tafel curves from the potentiodynamic polarization tests of Zn foil in PFZ electrolyte show higher corrosion potential and lower corrosion current than that in traditional $ZnSO_4$ aqueous electrolyte (figure 1(g)) [33]. Specifically, the corrosion potential of Zn in PFZ increased by ∼2.3 mV (from 14.6 mV to 16.9 mV), while the corrosion current decreased significantly from −1.06 mA in $ZnSO_4$ to −2.2648 mA, indicating that Zn in PFZ experiences much lower corrosion rate than in the aqueous environment. These results further suggest the advantages of PFZ for Zn batteries.

The ionic conductivity of solid-state electrolytes stands as a critical indicator for their applications in solid-state batteries. The ionic conductivity of PFZ over the room temperature range was measured using EIS, figure 1(h), revealing a good Zn^{2+} conductivity of 2.06×10^{-4} S cm^{-1} based on the following equation (1)

$$\sigma = \frac{d}{(\mathrm{RCT} - \mathrm{RS}) * S} \tag{1}$$

where 'σ' denotes the conductivity of PFZ, 'R' signifies resistance obtained from the impedance spectrum (Ω) and 'S' represents the effective area coated with silver paste (cm^2), 'd' stands for PFZ thickness (cm, obtained from SEM image, figures S10 and S11). R_{CT} is the electron transfer resistance across the electrode at the electrode-electrolyte interface and R_S is the resistance between the working electrode and the reference electrode (Note: in our 2-electrode system, the counter electrode acts as reference electrode). A lower resistance implies better zinc ion transferability. Weight retention comparisons between 2 M $ZnSO_4$ aqueous solution and PFZ (figure S12) after continuous heating at 50 °C for 20 h reveal significant weight loss in the former, addressing the traditional issue of replenishing electrolyte in aqueous zinc batteries and enhancing the potential of PFZ for practical applications.

3.2. Electrochemical performance of symmetrical cells

To understand PFZ's effects on zinc surface, symmetrical coin cells with zinc foils as electrodes were assembled and evaluated under galvanostatic conditions with a fixed plating time of 1 h. Given PFZ's relative softness and mechanical instability, glass fiber (GF) was used as the support holder for the electrolyte during galvanostatic cycle tests (figures S13 and S14). At a charge current density of 0.2 mA cm^{-2} (figure 2(a)), the aqueous ZnI_2 battery experienced a short circuit after 300 h due to the sharp zinc dendrites and undesirable HER and the detail of this duration is in figure S15. In contrast, owing to the smoother zinc surface and hydrogen-free characteristics enabled by the as-developed PFZ electrolyte with the improved zinc deposition and suppressed HER in the ZnI_2 battery, maintain steady cycles for approximately 5000 h (figure 2(a)). Intriguingly, the voltage polarization of the solid-state ZnI_2 battery exhibits a notably lower initial nucleation overpotential (η) of approximately 24 mV compared to the conventional aqueous ZnI_2 battery, which shows an overpotential of around 68 mV. This distinction is illustrated in figures 2(b) and (c), focusing on nucleation overpotential and voltage polarization at a current density of 0.2 mA cm^{-2} (inset of figure 2(a)). Smaller η values indicate reduced nucleation resistance and local current density, suggesting a potential mitigation of dendrite accumulation [34, 35]. This phenomenon has the potential to enhance reversible plating/stripping behaviors and improve coulombic efficiency during prolonged battery cycling [36, 37]. The symmetrical solid-state ZnI_2 battery displayed stable polarization of about 30 mV at the 4000^{th} hour, probably due to the homogenized ion distribution facilitated by the fluoride-rich interlayer formed from the PFZ electrolyte. Another possible factor is the *in situ* formation of zinc fluoride (ZnF_2) matrix on the surface of the Zn foil, which can regulate interfacial Zn^{2+} flux [38, 39].

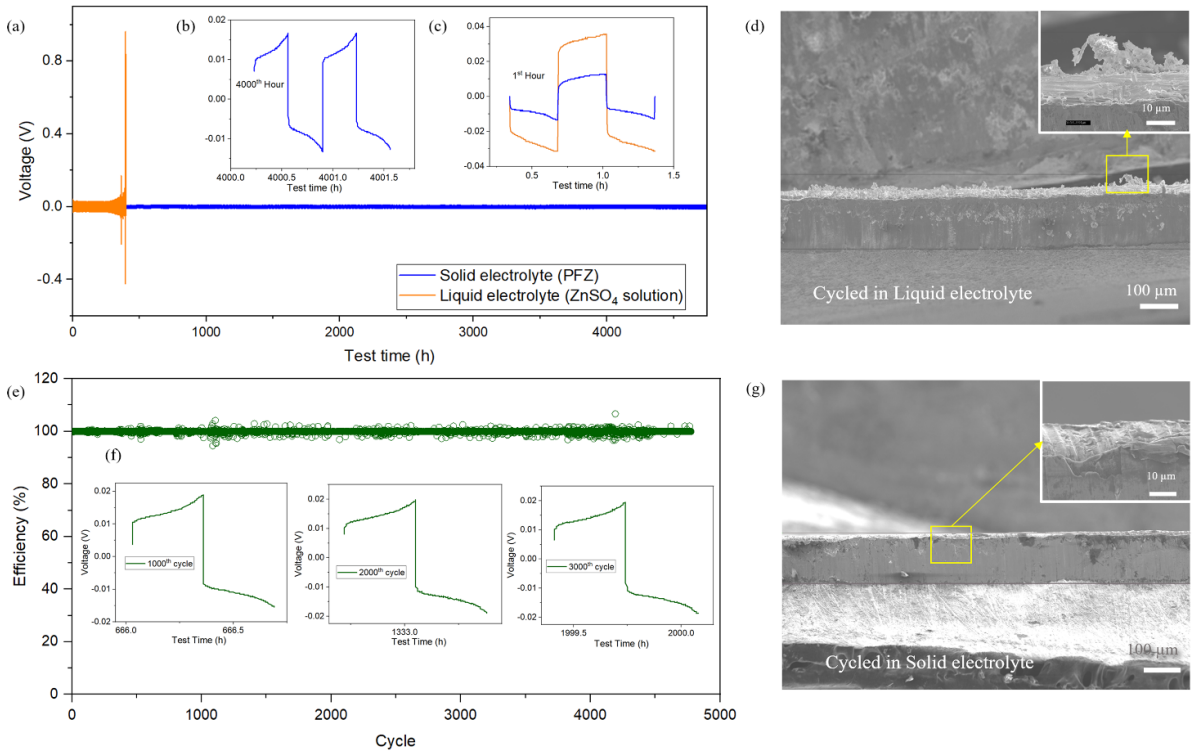

Figure 2. Symmetric batteries performance. (a) Galvanostatic Zn plating and stripping in Zn//$ZnSO_4$//Zn and Zn//PFZ//Zn symmetrical batteries at current densities of 0.2 mA cm^{-2}. The inset is the voltage profile of symmetrical cell at (b)1st hour, (c) 4000th hour. SEM images of cross-section of the zinc foil cycled in (d) 2 M $ZnSO_4$ aqueous solution and g) PFZ. (e) Coulombic efficiency of Zn deposition at the current density of 0.2 mA cm^{-2} and (f) the details of 1000th cycle, 2000th cycle and 3000th cycle.

Upon disassembling batteries cycled for 300 cycles with different electrolytes, the zinc foil showed notable morphology change in their SEM images. Figure 2(d) displayed clear zinc dendrites with sharp edges on the zinc surface cycled in the 2 M $ZnSO_4$ aqueous solution. In contrast, a smooth zinc surface without zinc dendrites was observed in the solid-state battery with PFZ electrolyte (figure 2(g)), mitigating the separator piercing caused by zinc dendrites for improved cycle stability. Furthermore, a stable coulombic efficiency of over 99% over 4000 cycles indicated near-complete recovery of deposited Zn in the subsequent stripping process (figure 2(e)) and the details of different cycles are shown in figure 2(f). This substantiates PFZ's efficacy as a superior electrolyte enabling reversible and durable zinc anodes.

3.3. Full solid-state Zn//PFZ//I_2 batteries performance

ZnI_2 full batteries were assembled to further validate PFZ facilitation of zinc ion transfer. In these batteries, the zinc metal foil serves as the anode, while PFZ functions as the electrolyte. Iodine adsorbed by nitrogen-doped CMK-3 carbon, termed CMK-N@I_2, is used as the cathode material. After five cycles, SEM analysis was conducted on the cross-section of the CMK-N@I_2. Revealing zinc signal peaks within the electrode (figure S16). Elemental analysis of four random locations consistently indicated the presence of zinc (figure S16), confirming the zinc transfer capability of PFZ and its role in facilitating reversible zinc anode reactions. The long-term cycle stability of ZnI_2 batteries using PFZ was investigated by galvanostatic charge/discharge measurements at 0.5 C (figure 3(a)), exhibiting a high coulombic efficiency of ∼100% and a specific capacity of 151.3 mAh g^{-1} over 7000 cycles (more than 10 000 h). These results underscored PFZ's contribution to stabilizing and enabling reversible Zn anodes. The voltage profiles across different cycles (figure 3(b)) displayed sustained cycle performance with a high capacity retention rate of 72.2%. The rate performance of ZnI_2 batteries, reflective of zinc ion migration, electrolytes, and interface effects on charge/discharge rates [40], demonstrated the superior performance of solid-state Zn//PFZ//I_2 batteries (figure 3(c)). Various charge/discharge conditions from 0.5 C to 20 C revealed impressive discharge capacities of 209.5, 179.6, 148.5, 106.9 and 79.8 mAh g^{-1}, respectively. Even at an ultrahigh current density of 20 C, the battery can still deliver a reversible capacity of 79.8 mAh g^{-1} which is significantly higher than other ZnI_2 batteries with gel electrolyte (figure 3(d)) [1, 41–43]. The discharge capacity recovered to 172.4 mAh g^{-1} immediately at 0.5 C after high-current density discharge, showcasing exceptional rate capability. In addition, the electrochemical reaction kinetics of ZnI_2 solid-state batteries were analyzed by scanning voltammetry at different scan rates. Figure 3(F) presents the CV curves of the

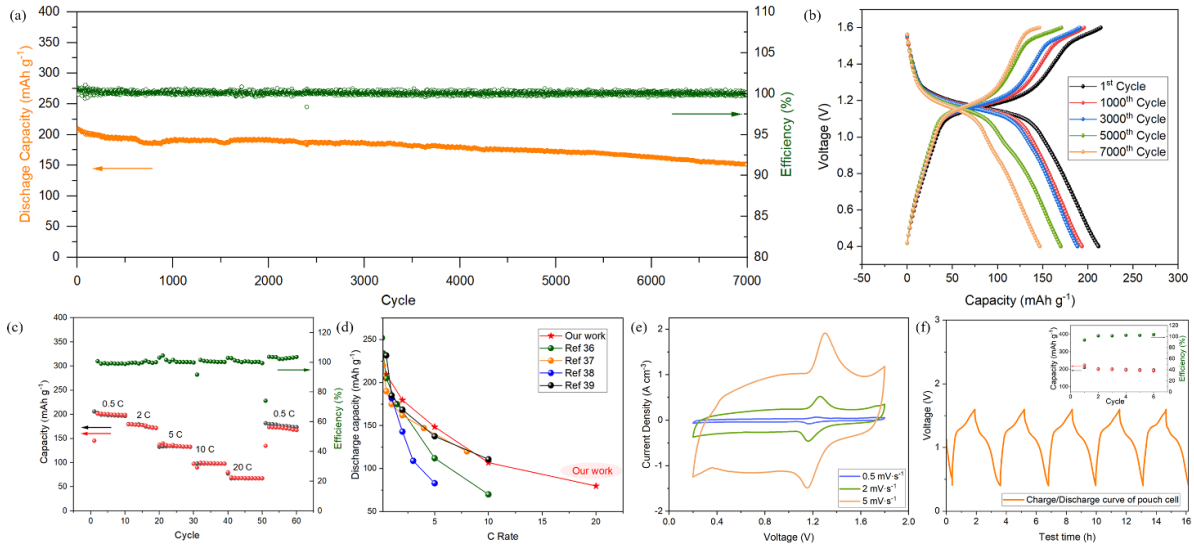

Figure 3. Full solid-state Zn//PFZ//I_2 batteries performance. (a) Cycle stability and coulombic efficiency of Zn//PFZ//I_2 battery at 0.5 C. (b) Voltage profiles at different cycles of Zn//PFZ//I_2 battery. (c) Rate performance and charge/discharge profiles of the Zn//PFZ//I_2 battery at current densities varying from 0.5 C to 20 C. (d) Rate performance comparison with other zinc iodine batteries with gel electrolyte. (e) CV curves at different scan rates of 0.5 mV s^{-1}, 2 mV s^{-1}, and 5 mV s^{-1}. (f) First 6 cycles charge/discharge curve of Zn//PFZ//I_2 soft-pack battery.

Zn//PFZ//I_2 battery at 3 different scan rates in the voltage range of 0.4–1.8 V. As the scan rate increased, peak potential differences and peak currents (i) rose accordingly, indicating reversible Zn^{2+} plating and stripping. As the scan rate increases, the difference between charge/discharge does not change, which indicates that the polarization of the battery is small and echoes the good ionic conductivity mentioned above. Taking the advantage of the flexibility of PFZ solid-state electrolyte, 100 mg-level soft-pack Zn//PFZ//I_2 batteries were assembled (figure S17), which are capable of powering light-emitting diodes (LEDs) and maintaining normal open circuit voltage even after being folded to 180 degrees (figure S18). Furthermore, unlike the pouch cell with 2 M $ZnSO_4$ aqueous solution, those flexible solid-state batteries with PFZ exhibited no swelling after 500 cycles (figure S19), confirming a gas-free charging/discharging process. Specific cycle curves (figure 3(f)) further supported the stability and reversibility of Zn//PFZ//I_2 batteries, emphasizing PFZ's crucial role in prolonging battery lifespan and its potential for portable and flexible applications.

3.4. Effects on I_3^- shuttling process in ZnI_2 batteries

The polyiodide shuttle remains another challenge in ZnI_2 batteries, contributing to substantial active material loss, zinc anode corrosion, and reduced battery cycle life [31, 40]. The compact structure of solid-state electrolytes theoretically mitigates the impact on shuttle effect. An H-shaped cell was applied to visualize the I_3^- shuttle process (figure 4(a)). The left container was filled with deep brown triiodide solution and iodine element, while the right side held colorless iodized salt solution. As GF is widely used as the separator in aqueous Zn battery, it is used as the separator for the H-cell experiment. Within 1 min, the solution in the right container turned brown, indicating I_3^- passing through the large pores of GF (figure 4(a)). In sharp contrast, when PFZ was used as the separator, solution in the right chamber turned to light yellow after 12 h, highlighting significantly lowered I_3^- shuttle rates compared to that in the traditional GF separator. (figures 4(b) and (c) displayed increasing I_3^- concentration with extended rest times [44]. The inhibited I_3^- shuttling stands as a primary reason for the enhanced performance of Zn//PFZ//I_2 batteries [45]. In order to accurately express the I_3^- concentration changes in the right container of the H-type cell, ultraviolet-visible spectroscopy (UV–vis) tests on the solution in the right container at different time scales were conducted. The calculated results based on the UV–vis data and standard curves are shown in table S3. When the solution separated by the traditional GF separator was diluted 2000 times, the solution separated by PFZ underwent a 10-fold dilution. PFZ can notably reduce the shuttle effect of I_3^- in ZnI_2 batteries, and the inhibited I_3^- shuttling stands as a primary reason for the enhanced performance of Zn//PFZ//I_2 batteries [46]. The results in the H-cell experiment are in accordance with the post-mortem XPS analysis on the zinc electrodes cycled in different electrolyte environments. GF separators in a liquid environment failed to prevent polyiodide ions penetration, as evidenced by iodine presence after etching (figures 4(d) and (e)). Conversely, no iodine was detected on zinc foil cycled in the solid PFZ electrolyte, suggesting the effectively prevented shuttle effect of iodine. Furthermore, the influence of the I_3^- shuttle effect on battery self-discharge was studied by introducing a static process into the normal charge-discharge cycle test. As shown in figures 4(f) and (g), after five cycles and a

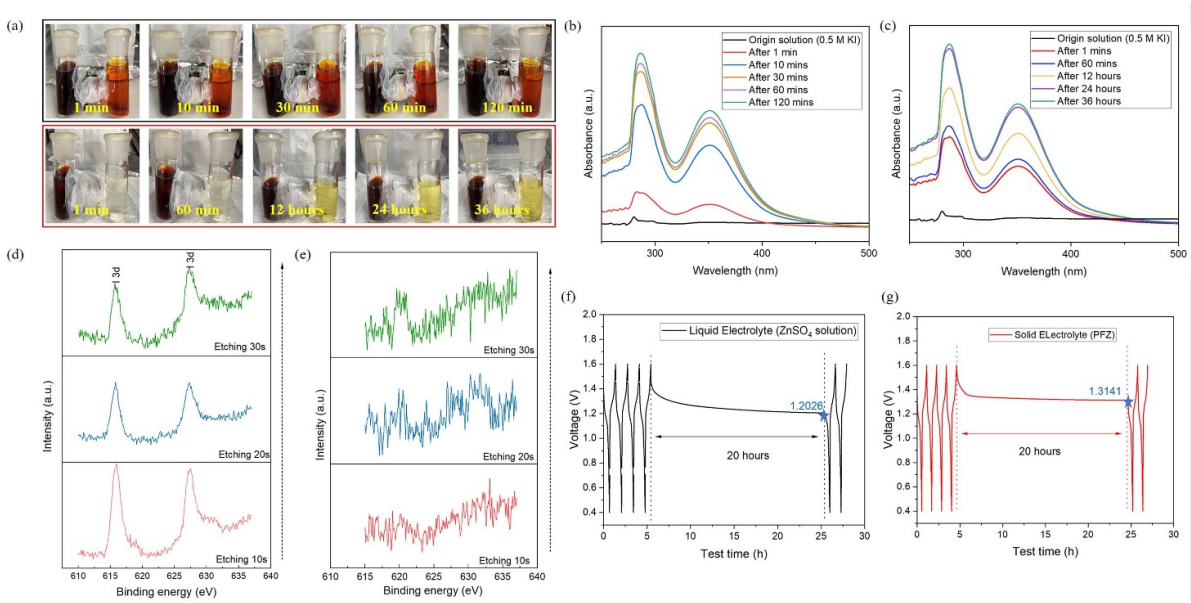

Figure 4. Effects on I_3^- shuttling process in ZnI_2 batteries. (a) Photographs of H-shape tanks containing a deep brown triiodide solution (1 M KI + 0.1 M I_2, left tank) and a colorless 0.5 M KI solution (right tank), each separated by either a GF separator or PFZ at various time intervals. (b), (c) UV–vis curve of solution in the H-shape right tanks after different time using different separators (GF separator and PFZ). (d) I 3d XPS spectra of Zn surface cycled 10 times with GF as separator etched by 10 keV Ar^+ as a function of etching time. (e) I 3d XPS spectra of Zn surface cycled 10 times with PFZ as separator etched by 10 keV Ar^+ as a function of etching time. (f), (g) Voltage drops in charge-discharge cycling and self-discharge tests of (f) aqueous ZnI_2 battery and (g) solid-state ZnI_2 battery.

20 hour stand at 1.6 V, the voltage of the aqueous ZnI_2 battery dropped to 1.2026 V, in comparison to that of 1.3141 V in the battery equipped with PFZ electrolyte. The dramatically suppressed self-discharge by using the solid-state PFZ electrolyte will aid practical battery applications.

3.5. Zinc electrode (anode) surface analysis

To delve into the influence of PFZ electrolyte on zinc surface, a comparative analysis was conducted between an aqueous ZnI_2 battery using a 2 M $ZnSO_4$ aqueous solution and a solid-state ZnI_2 battery employing PFZ as the electrolyte. Zinc anodes were obtained by disassembling batteries subjected to various states of charge and discharge (25% S.O.C., 50% S.O.C., 100% S.O.C., 50% S.O.D. and 25% S.O.D.) for XRD analysis. In the XRD pattern of Zn electrode cycled under 2 M $ZnSO_4$ aqueous electrolyte (figure 5(a)), the strengthened diffraction peaks of $Zn(OH)_2$ during charging signify the gradual corrosion of the zinc metal surface by water in the electrolyte by forming a passivation layer containing $ZnSO_4(OH)_6{\cdot}xH_2O$ and $Zn(OH)_2$ [47–49]. This passivation layer adversely affects zinc plating and results in zinc wastage. In contrast, no characteristic peaks of $Zn(OH)_2$ were observed in PFZ-based batteries (figure 5(b)), indicating that PFZ can reduce metal anode corrosion for enhanced battery performance. Then, the growth of zinc dendrites was visually identified by investigating the surface morphology of the zinc foil after 100 cycles at 0.5 mA cm^{-2} in the symmetric batteries. As shown in figure 5(c), the zinc foil surface cycled in 2 M $ZnSO_4$ aqueous solution is covered with vertically grown zinc dendrites, which could penetrate the separator, eventually leading to short circuit. In contrast, after 100 cycles, the zinc surface cycle with PFZ exhibited a dense and dendrite-free morphology (figure 5(d)).

Further XRD tests on the zinc foils cycled in the Zn//PFZ//Zn symmetric battery for 5, 50 and 500 cycles unveiled new characteristic peaks around 27, 34, 42 and 52 degrees (figure 5(e)), indicating the emergence of zinc fluoride (ZnF_2) along with battery cycling [50]. This suggests the formation of a new ZnF_2 substance with zinc plating and stripping in the PFZ electrolyte. Subsequent XPS tests on zinc foil cycled for five times in Zn//PFZ//Zn symmetric battery revealed an additional F 1 s hump ($\approx$ 683.8 eV), confirming the formation of the ZnF_2 interlayer (figures 5(f) and (g)) [51]. Similarly, the Zn spectra display a broader pair of peaks, distinguishable into two signals. One corresponds to the Zn origin peak, while the other one corresponds to the Zn-F polar bonds, each exhibiting distinct binding energies [52, 53]. Furthermore, Raman spectroscopy in figure 5(h) showcases a distinct characteristic peak of ZnF_2 around 520 cm^{-1} [54]. In contrast, the surface of the Zn foil in a battery with a 2 M $ZnSO_4$ aqueous solution electrolyte mostly contained Zn oxides, hydroxides, and complex sulfate-containing hydrates (figure S20). This validates earlier assertions regarding the ZnF_2 SEI layer's role in achieving longer and more stable cycle performance, as discussed in Part 3.2.

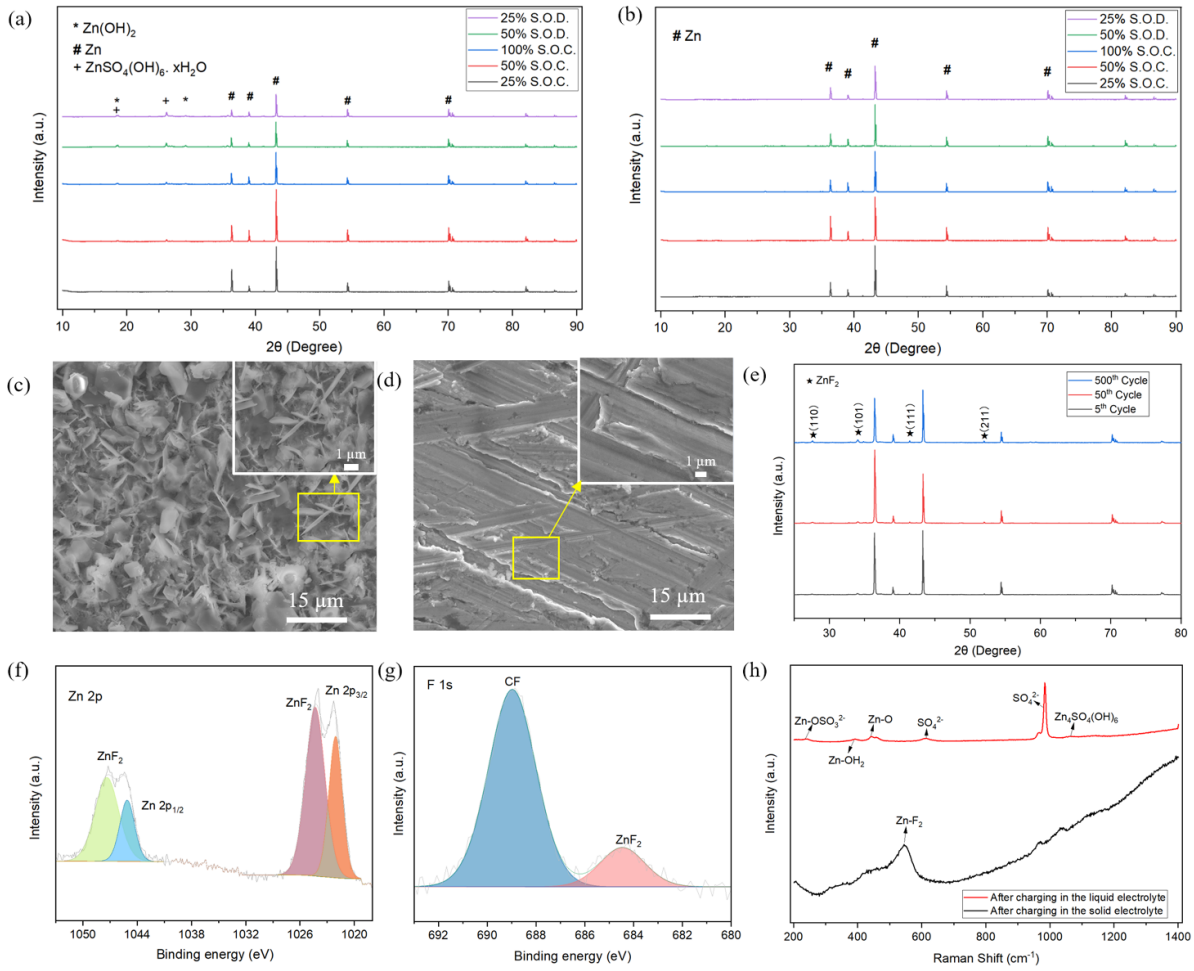

Figure 5. Characterization of metallic Zn electrode. XRD patterns of Zn anodes at various states of charge and discharge cycled in (a) 2 M $ZnSO_4$ aqueous solution and (b) PFZ. SEM images of Zn anode cycled in (c) 2 M $ZnSO_4$ aqueous solution and (d) PFZ at 0.5 mA cm^{-2} in the Zn//PFZ//Zn symmetric battery. (e) XRD patterns of Zn anode cycled 5, 50 and 500 times in PFZ. (f), (g) XPS results of Zn anode cycled 5 times in Zn//PFZ//Zn symmetric battery. (h) Raman spectroscopy of Zn anode cycled in 2 M $ZnSO_4$ aqueous solution and PFZ.

4. Conclusion

In this study, we successfully synthesized a novel solid-state electrolyte, PFZ, by incorporating a PFPE-based polymer (PF) with zinc salt. Our research has shown that PFZ not only boasts exceptional ionic conductivity but also outperforms conventional aqueous ZnI_2 batteries in terms of electrochemical performance. A key advantage of the PFZ electrolyte lies in its ability to facilitate the formation of a protective SEI film enriched with zinc fluoride on the zinc foil surface, which effectively mitigates the growth of zinc dendrites and significantly prolongs the cycle life of the battery (over 7000 stable cycles with capacity retention exceeding 72.2%). Furthermore, the compact structure of the PFZ electrolyte combats the detrimental shuttle effect caused by the migration of multiple iodide ions within the battery. The excellent rate capability of the ZnI_2 solid-state battery further underscores its potential for efficient industrial applications. The findings presented in this study emphasize the promising potential of PFZ as a solid-state electrolyte for ZnI_2 batteries, paving the way for improved battery performance, longevity, and wider industrial utilization.

5. Future perspective

In the future, as researchers continue to delve deeper into the realm of solid-state electrolytes, the development of novel materials and fabrication techniques will play a pivotal role in overcoming the persistent challenges faced by aqueous batteries. The integration of solid polymer-based electrolytes represents a promising avenue for enhancing battery performance and safety, paving the way for the widespread adoption of Zn-I_2 batteries in diverse applications. Looking ahead, efforts should focus on further optimizing the design and composition of solid electrolytes to maximize ion conductivity while minimizing interface resistance. Additionally, exploring the synergistic effects of electrolyte engineering with advanced electrode materials holds immense potential for unlocking new frontiers in energy storage technology. Furthermore, the

scalability and cost-effectiveness of solid-state Zn-I_2 batteries will be crucial considerations for their commercial viability and widespread deployment. Continued collaboration between academia, industry, and government agencies will be essential in driving forward the research agenda and translating scientific discoveries into real-world solutions. By addressing these challenges and seizing opportunities for innovation, the future holds great promise for solid-state Zn-I_2 batteries as a cornerstone of sustainable energy storage systems, powering the transition towards a greener and more resilient future.

Acknowledgments

The authors were grateful for the financial support of the Australian Research Council through their Fellowships (FT200100279 and DE230101105), Discovery (DP230100572), and Linkage Programs (LP220100036). The authors also acknowledge the scientific and technical support from the Australian Microscopy & Microanalysis Research Facility at the Centre for Microscopy and Microanalysis, the University of Queensland. The Australian National Fabrication Facility, Queensland Node is acknowledged for access to some items of equipment.

Conflict of interest

The authors declare no conflict of interest.

Author contributions

Y Huang and Y Wang contributed equally to this work. Y Huang conceived this work and conducted device fabrication and electrochemical measurements. Y, Wang carried out the material synthesis and characterisations. B Luo and C Zhang obtained funding and supervised the project. T Lin, X Huang, N, Alghamdi, M Rana, P Chen, supported the experiments and discussed the results. Y Huang and Y Wang wrote the manuscript with further revision from C Zhang, A Whittaker, L Wang, and B Luo. All authors have commented on the work.

ORCID iD

Bin Luo https://orcid.org/0000-0003-2088-6403

References

[1] Sonigara K K, Zhao J, Machhi H K, Cui G and Soni S S 2020 Self-assembled solid-state gel catholyte combating iodide diffusion and self-discharge for a stable flexible aqueous Zn-I2 battery *Adv. Energy Mater.* **10** 2001997
[2] Guo Q, Wang H, Sun X, Yang Y, Chen N and Qu L 2022 *In situ* synthesis of cathode materials for aqueous high-rate and durable Zn-I2 batteries *ACS Mater. Lett.* **4** 1872
[3] Zou Y, Liu T, Du Q, Li Y, Yi H, Zhou X, Li Z, Gao L, Zhang L and Liang X 2021 A four-electron Zn-I2 aqueous battery enabled by reversible I-/I2/I+ conversion *Nat. Commun.* **12** 170
[4] Wang F, Tseng J, Liu Z, Zhang P, Wang G, Chen G, Wu W, Yu M, Wu Y and Feng X 2020 A stimulus-responsive zinc-iodine battery with smart overcharge self-protection function *Adv. Mater.* **32** 2000287
[5] Yang H, Qiao Y, Chang Z, Deng H, He P and Zhou H 2020 A metal-organic framework as a multifunctional ionic sieve membrane for long-life aqueous zinc-iodide batteries *Adv. Mater.* **32** 2004240
[6] Shin J, Lee J, Park Y and Choi J W 2020 Aqueous zinc ion batteries: focus on zinc metal anodes *Chem. Sci.* **11** 2028
[7] Yang X, Zhang Z, Wu M, Guo Z-P and Zheng Z-J 2023 Reshaping zinc plating/stripping behavior by interfacial water bonding for high-utilization-rate zinc batteries *Adv. Mater.* **35** 2303550
[8] Naveed A, Rasheed T, Raza B, Chen J, Yang J, Yanna N and Wang J 2022 Addressing thermodynamic instability of Zn anode: classical and recent advancements *Energy Storage Mater.* **44** 206
[9] Liang P, Yi J, Liu X, Wu K, Wang Z, Cui J, Liu Y, Wang Y, Xia Y and Zhang J 2020 Highly reversible Zn anode enabled by controllable formation of nucleation sites for Zn-based batteries *Adv. Funct. Mater.* **30** 1908528
[10] Wang W, Chen S, Liao X, Huang R, Wang F, Chen J, Wang F, Wang H and Wang Y 2023 Regulating interfacial reaction through electrolyte chemistry enables gradient interphase for low-temperature zinc metal batteries *Nat. Commun.* **14** 5443
[11] Naveed A, Ali A, Rasheed T, Wang X, Ye P, Li X, Zhou Y, Mingru S and Liu Y 2022 Revisiting recent and traditional strategies for surface protection of Zn metal anode *J. Power Sources* **525** 231122
[12] Xie C, Liu Y, Lu W, Zhang H and Li X 2019 Highly stable zinc-iodine single flow batteries with super high energy density for stationary energy storage *Energy Environ. Sci.* **12** 1834
[13] Tang B, Shan L, Liang S and Zhou J 2019 Issues and opportunities facing aqueous zinc-ion batteries *Energy Environ. Sci.* **12** 3288
[14] Han D *et al* 2020 A corrosion-resistant and dendrite-free zinc metal anode in aqueous systems *Small* **16** 2001736
[15] Zhao K, Wang C, Yu Y, Yan M, Wei Q, He P, Dong Y, Zhang Z, Wang X and Mai L 2018 Ultrathin surface coating enables stabilized zinc metal anode *Adv. Mater. Interfaces* **5** 1800848
[16] Mathew V, Schorr N B, Sambandam B, Lambert T N and Kim J 2023 A critical comparison of mildly acidic versus alkaline zinc batteries *Acc. Mater. Res.* **4** 299
[17] Quartarone E and Mustarelli P 2011 Electrolytes for solid-state lithium rechargeable batteries: recent advances and perspectives *Chem. Soc. Rev.* **40** 2525
[18] Manthiram A, Yu X and Wang S 2017 Lithium battery chemistries enabled by solid-state electrolytes *Nat. Rev. Mater.* **2** 16103
[19] Kato Y, Hori S, Saito T, Suzuki K, Hirayama M, Mitsui A, Yonemura M, Iba H and Kanno R 2016 High-power all-solid-state batteries using sulfide superionic conductors *Nat. Energy* **1** 16030
[20] Liu Q, Liu R, He C, Xia C, Guo W, Xu Z-L and Xia B Y 2022 Advanced polymer-based electrolytes in zinc–air batteries *eScience* **2** 453
[21] Xie K, Ren K, Wang Q, Lin Y, Ma F, Sun C, Li Y, Zhao X and Lai C 2023 In situ construction of zinc-rich polymeric solid–electrolyte interface for high-performance zinc anode *eScience* **3** 100153
[22] Ferguson C J, Hughes R J, Nguyen D, Pham B T T, Gilbert R G, Serelis A K, Such C H and Hawkett B S 2005

Ab initio emulsion polymerization by RAFT-controlled self-assembly *Macromolecules* **38** 2191
[23] Zhang C *et al* 2017 PFPE-based polymeric 19F MRI agents: a new class of contrast agents with outstanding sensitivity *Macromolecules* **50** 5953
[24] Wang X *et al* 2022 Ultra-stable all-solid-state sodium metal batteries enabled by perfluoropolyether-based electrolytes *Nat. Mater.* **21** 1057
[25] Dueramae I, Okhawilai M, Kasemsiri P and Uyama H 2021 High electrochemical and mechanical performance of zinc conducting-based gel polymer electrolytes *Sci. Rep.* **11** 13268
[26] Li Y, Wang Z, Li W, Zhang X, Yin C, Li W, Guo K, Zhang X and Wu J 2023 Trinary nanogradients at electrode/electrolyte interface for lean zinc metal batteries *Energy Storage Mater.* **61** 102873
[27] Saal A, Hagemann T and Schubert U S 2021 Polymers for battery applications—active materials, membranes, and binders *Adv. Energy Mater.* **11** 2001984
[28] Stolwijk N A, Heddier C, Reschke M, Wiencierz M, Bokeloh J and Wilde G 2013 Salt-concentration dependence of the glass transition temperature in PEO-NaI and PEO-LiTFSI polymer electrolytes *Macromolecules* **46** 8580
[29] Zhu Y, Yang G and Zhou H 2022 An aqueous zinc-ion battery working at −50 °C enabled by low-concentration perchlorate-based chaotropic salt electrolyte *EcoMat* **4** e12165
[30] Bard A J, Inzelt G and Scholz F (eds) 2008 E BT *Electrochemical Dictionary* (Springer) pp 175–264
[31] Huo S, Sheng L, Xue W, Wang L, Xu H, Zhang H and He X 2023 Challenges of polymer electrolyte with wide electrochemical window for high energy solid-state lithium batteries *InfoMat* **5** e12394
[32] Tian H *et al* 2022 Three-dimensional Zn-based alloys for dendrite-free aqueous Zn battery in dual-cation electrolytes *Nat. Commun.* **13** 7922
[33] Shang W *et al* 2021 Establishing high-performance quasi-solid Zn/I2 batteries with alginate-based hydrogel electrolytes *ACS Appl. Mater. Interfaces* **13** 24756
[34] Yuan L, Hao J, Johannessen B, Ye C, Yang F, Wu C, Dou S, Liu H and Qiao S 2023 Hybrid working mechanism enables highly reversible Zn electrodes *eScience* **3** 100096
[35] Hou Z and Zhang B 2022 A solid-to-solid metallic conversion electrochemistry toward 91% zinc utilization for sustainable aqueous batteries *EcoMat* **4** e12265
[36] Pei A, Zheng G, Shi F, Li Y and Cui Y 2017 Nanoscale nucleation and growth of electrodeposited lithium metal *Nano Lett.* **17** 1132
[37] Wu X, Dai Y, Li N W, Chen X C and Yu L 2024 Recent progress in ionic liquid-based electrolytes for nonaqueous and aqueous metal batteries *eScience* **4** 100173
[38] Wang Y, Wu Z, Azad F M, Zhu Y, Wang L, Hawker C J, Whittaker A K, Forsyth M and Zhang C 2024 Fluorination in advanced battery design *Nat. Rev. Mater.* **9** 119
[39] Yang Y, Liu C, Lv Z, Yang Y, Zhang H, Ye M, Chen L, Zhao J and Li C C 2021 Synergistic manipulation of Zn2+ ion flux and desolvation effect enabled by anodic growth of a 3D ZnF2 matrix for long-lifespan and dendrite-free zn metal anodes *Adv. Mater.* **33** 2007388
[40] Zeng Y *et al* 2023 Extreme fast charging of commercial Li-ion batteries via combined thermal switching and self-heating approaches *Nat. Commun.* **14** 3229
[41] Yang J *et al* 2023 Hetero-polyionic hydrogels enable dendrites-free aqueous Zn-I2 batteries with fast kinetics *Adv. Mater.* **35** 2306531
[42] Wang M, Ma J, Zhang H, Fu L, Li X and Lu K Bidirectional confined redox catalysis manipulated quasi-solid iodine conversion for shuttle-free solid-state Zn-I2 battery *Small* **2023** 2307021
[43] Machhi H K, Sonigara K K, Bariya S N, Soni H P and Soni S S 2021 Hierarchically porous metal–organic gel hosting catholyte for limiting iodine diffusion and self-discharge control in sustainable aqueous Zinc-I2 batteries *ACS Appl. Mater. Interfaces* **13** 21426
[44] Zhang S, Hao J, Li H, Zhang P, Yin Z, Li Y, Zhang B, Lin Z and Qiao S 2022 Polyiodide confinement by starch enables shuttle-free zn-iodine batteries *Adv. Mater.* **34** 2201716
[45] Yang J, Liu H, Zhao X, Zhang K, Zhang X, Ma M, Gu Z, Cao J and Wu X 2024 Janus binder chemistry for synchronous enhancement of iodine species adsorption and redox kinetics toward sustainable aqueous Zn-I2 batteries *J. Am. Chem. Soc.* **146** 6628
[46] Ma L, Ying Y, Chen S, Huang Z, Li X, Huang H and Zhi C 2021 Electrocatalytic iodine reduction reaction enabled by aqueous zinc-iodine battery with improved power and energy densities *Angew. Chem., Int. Ed.* **60** 3791
[47] Ghica D, Vlaicu I D, Stefan M, Maraloiu V A, Joita A C and Ghica C 2019 Tailoring the dopant distribution in zno: mn nanocrystals *Sci. Rep.* **9** 6894
[48] Hou Z, Zhang T, Liu X, Xu Z, Liu J, Zhou W, Qian Y, Fan H J, Chao D and Zhao D 2023 A solid-to-solid metallic conversion electrochemistry toward 91% zinc utilization for sustainable aqueous batteries *Sci. Adv.* **8** eabp8960
[49] Meng C, He W, Tan H, Wu X, Liu H and Wang J 2023 A eutectic electrolyte for an ultralong-lived Zn//V_2O_5 cell: an in situ generated gradient solid-electrolyte interphase *Energy Environ. Sci.* **16** 3587
[50] An Y, Tian Y, Zhang K, Liu Y, Liu C, Xiong S, Feng J and Qian Y 2021 Stable aqueous anode-free zinc batteries enabled by interfacial engineering *Adv. Funct. Mater.* **31** 2101886
[51] Tao S *et al* 2022 A hydrophobic and fluorophilic coating layer for stable and reversible aqueous zinc metal anodes *Chem. Eng. J.* **446** 136607
[52] Cao L *et al* 2021 Fluorinated interphase enables reversible aqueous zinc battery chemistries *Nat. Nanotechnol.* **16** 902
[53] Ma L, Li Q, Ying Y, Ma F, Chen S, Li Y, Huang H and Zhi C 2021 Toward practical high-areal-capacity aqueous zinc-metal batteries: quantifying hydrogen evolution and a solid-ion conductor for stable zinc anodes *Adv. Mater.* **33** 2007406
[54] Han D *et al* 2022 A non-flammable hydrous organic electrolyte for sustainable zinc batteries *Nat. Sustain.* **5** 205